文章编号：1001－9014(2016)06－0656－06

DOI:10.11972/j.issn.1001－9014.2016.06.004

Passive submillimeter-wave imaging demonstrated by a two-element interferometer

HAN Dong-Hao[1,2], LIU Hao[1*], ZHANG De-Hai[1], MENG Jin[1], ZHAO Xin[1], ZHANG Ying[1,2], WU Ji[1]

(1. National Space Science Center, Chinese Academy of Sciences, Beijing 100190, China;
2. University of Chinese Academy of Sciences, Beijing 100049, China)

Abstract: In this paper, an SMMW interferometric radiometer concept is demonstrated by a two-element interferometer with dedicated high accuracy SMMW devices. Point-source calibration method is introduced in order to reduce instrument errors. Interference fringes and point target images are presented by this SMMW interferometer. The linear phase error of the interference fringes is less than 2° and the angular resolution is better than 0.57°. The measured performance characteristics of the two-element interferometer are consistent with the theoretical analysis. This interferometer demonstrates a new method for passive SMMW remote sensing.

Key words: submillimeter-wave (SMMW) imaging, point-source calibration, SMMW interference fringes, interferometric imaging

PACS: 07.57.Kp

干涉式被动亚毫米波成像系统

韩东浩[1,2], 刘 浩[1*], 张德海[1], 孟 进[1], 赵 鑫[1], 张 颖[1,2], 吴 季[1]

(1. 中国科学院国家空间科学中心 微波遥感重点实验室,北京 100190;
2. 中国科学院大学,北京 100049)

摘要:通过特殊设计的高精度SMMW器件,实现了一套基于二单元干涉仪的干涉式辐射计系统.针对该系统的自身特点,作者提出了点源目标响应定标方法来降低系统误差.系统完成后,分别进行了干涉条纹实验和点源目标成像实验.经测试,系统的线性相位误差小于2°,角分辨率优于0.57°.系统实测性能和理论分析结果一致.以上研究为今后设计高分辨率亚毫米波干涉式成像辐射计提供了重要的参考价值.

关 键 词:亚毫米波成像;点源目标响应定标;亚毫米波干涉条纹;干涉式成像

中图分类号:TN454 **文献标识码**:A

Introduction

The submillimeter-wave (SMMW) spectral region with frequencies from 300 GHz to 3 000 GHz is one of the most interesting but challenging sectors of the electromagnetic spectrum. It is interesting because of the wealth of knowledge that can be gained from research at these frequencies, and challenging because the techniques used for research in this region lag behind those used at lower and higher frequencies[1]. Of late, as a result of the advancement of SMMW technology[2], SMMW sensors play an increasingly significant role in remote sensing applications,[3] such as security detection[4] and meteorological observations[5].

In geoscience applications[6], various molecules have characteristic absorption lines in the SMMW spectral region, including the water vapor absorption spectra at 380 GHz and the oxygen absorption spectra at 425 GHz. Several researches on the SMMW electromagnetic spectrum have been conducted with successes such as the Aura[7] and the Superconducting Submillimeter-Wave Limb-Emission Sounder (SMILES)[8]. The geostationary

Received date: 2016-03-21, **revised date**: 2016-09-30 **收稿日期**:2016-03-21, **修回日期**:2016-09-30

Foundation items: Supported by the National 863 Program (2013AA122701) and the Scientific Research Fund of the Meteorological Public Welfare Profession (GYHY201506023)

Biography: HAN Dong-Hao (1990-), male, Shandong, China, Ph. D. Research interests include sub-millimeter wave applications and the system design of synthetic aperture radiometers. E-mail: handonghao1124@163.com

* **Corresponding author**: E-mail: liuhao@mirslab.cn

interferometric microwave sounder (GIMS)[9] is a millimeter-wave imaging sounder concept proposed for the next generation Chinese geostationary meteorological satellite (FY-4M). Millimeter-wave (MMW) bands at 50 ~ 56 GHz and 183 GHz have been developed for the GIMS[10].

Most of the existing SMMW sensors are based on spatial domain scanning imaging or focal plane array imaging. Although a spatial domain scanning imaging system has a simple hardware structure, it has a large antenna aperture and a long imaging period, e. g., the Microwave Limb Sounder (MLS) in the Aura[7,11]. On the other hand, a focal plane array can reduce the imaging time but the hardware is expensive, e. g., the Heterodyne Instrument for the Far-Infrared (HIFI) in the Herschel[12]. Different from these instruments, the large antenna aperture will be synthetic by means of some small antennas in interferometric radiometers. For this reason, the interferometric radiometers are also known as synthetic aperture radiometers[13]. In this type of radiometer, spatial frequency domain sampling can be accomplished using mobile receivers, hence, there is a flexible tradeoff between the complexity of the system and the imaging period. Unlike traditional radiometers, the knowledge of the phase relationship between the receivers is important for correlation measurements in interferometric radiometers[14-15]. Therefore, a high degree of hardware stability and phase accuracy should be achieved in the SMMW spectral region because SMMW is highly sensitive to phase errors. To the best of our knowledge, the highest frequency achieved in existing interferometric imaging radiometers is 183 GHz in the Geostationary Synthetic Thinned Array Radiometer (GeoSTAR) project[16].

In this paper, a passive SMMW interferometric radiometer was setup with a two-element interferometer working at 440 GHz. Related SMMW devices with a high stability were developed in the interferometric radiometer to ensure hardware stability and phase accuracy in the SMMW spectral region[17-18]. In addition, a new calibration method, the point-source calibration, was introduced to eliminate instrument errors. In Sect. 1, the observations for the interferometric radiometer are formulated. In Sect. 2, the two-element SMMW interferometer and the point-source calibration method are presented. In Sect. 3, we demonstrate the interference fringes and the point target images obtained with this SMMW interferometer, followed by the conclusion and outlook in Sect. 4.

1　Formulation for interferometric imaging

The architecture of a two-element interferometer[13] is shown in Fig. 1. The two antennas were separated by a distance D and arranged to observe a point-source located at θ_0, which is in the far-field of the interferometer. Hence, the incident wavefront can be considered as a plane wave. In order to simplify the discussion, the receivers were assumed to have narrow bandpass filters that pass only the signal components that are very close to f_0.

The output V_i in Fig. 1 can be described as:

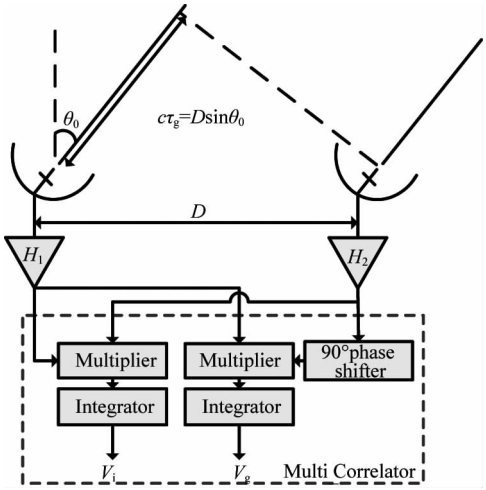

Fig. 1　Two element interferometer
图 1　二单元干涉仪

$$\begin{aligned} V_i &= < A(\theta_0)\sin(2\pi f_0 t + \varphi)A(\theta_0)\sin(2\pi f_0(t - \tau_g) + \varphi) > \\ &\propto A^2(\theta_0)\cos(2\pi f_0 \tau_g) \\ &= A^2(\theta_0)\cos(2\pi \frac{D}{\lambda}\sin\theta_0) \end{aligned} \quad , \quad (1)$$

where A is the signal strength of the point-source, λ is the wavelength corresponding to f_0, and τ_g is the time delay between the two receivers. The term V_q can be obtained in the same manner. When an distributed target expressed as $T(\xi,\eta)$ and bandwidths in the receivers are considered, the output of the two element interferometer shown in Fig. 1 can be described as[19]:

$$\begin{aligned} V(u,v) = \iint\limits_{\xi^2+\eta^2\leqslant 1} & \frac{T(\xi,\eta) - T_r}{\sqrt{1-\xi^2-\eta^2}} F_{1,2*}(\xi,\eta)\tilde{r}_{1,2} \\ & (-\frac{u\xi - v\eta}{f_0}) e^{-j2\pi(u\xi - v\eta)} d\xi d\eta \end{aligned} \quad , \quad (2)$$

where, (u,v) are the projections over the X-Y axes of the baseline D normalized to the wavelength. The term T_r is the instrument temperature, $F_{1,2*}(\xi,\eta)$ is the conjugate product of the receiver antenna pattern, and the two receivers are numbered 1 and 2, respectively. The term $\tilde{r}_{1,2}$ is the fringe washing function of the receiver frequency response[20]. V_q and V_i correspond to the real and imaginary parts of $V(u,v)$, respectively.

By changing the length and orientation of the baseline, $V(u,v)$ can be effectively sampled in spatial frequency domain by the two-element interferometer. Then, $T(\xi,\eta)$ can be retrieved by an appropriate inverse algorithm[21-22].

2　System architecture

The proposed SMMW interferometric radiometer was setup using a two-element interferometer. Because the SMMW is highly sensitive to delay errors, a high hardware stability and phase accuracy should be considered in SMMW interferometric radiometer. Hence, the SMMW devices used in the frontend should be elaborately de-

signed and a high-speed digital correlator was employed in the backend. In addition, we proposed a new calibration method, called the point-source calibration method, that can be used to reduce instrument errors.

2.1 Modular composition

This SMMW interferometer mainly consists of three parts: antenna part, SMMW frontend, and digital correlator. Further, a two-dimensional moving platform was employed to allow complete spatial frequency domain scanning. The overall system is shown in Fig. 2.

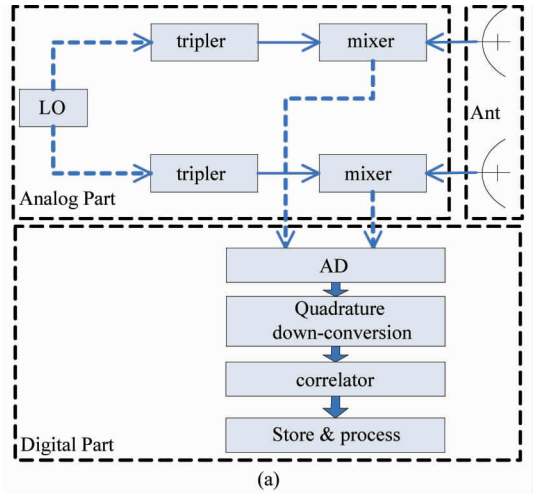

Fig. 2 SMMW interferometer (a) functional block diagram, (b) photo of the whole assembly

图 2 亚毫米波干涉仪 (a) 原理框图,(b) 装置实物照片

In Fig. 2(a), the dashed lines with arrows indicate flexible coaxial connections. Both of the receivers were mounted on the two moving arms of the moving platform. One arm can move horizontally and the other vertically, hence, the trace of these two arms is T-shaped and is called T-shaped scanning. The whole assembly of the SMMW interferometer and moving platform is shown in Fig. 2(b).

Horn antennas were employed in this system. The antenna gain is 25.6 dB, the 3 dB beam width is 10°, the sidelobe level is lower than -30 dB, and the cross polarization level is lower than -30 dB.

The analog part includes three main components: a local oscillator (LO), a tripler, and a mixer. A circuit structure of anti-parallel diodes with self-bias was proposed for the tripler[17], as shown in Fig. 3(a), which is an efficient way to realize odd-order frequency multiplication with bias circuit. The measured output power is maximum at 221 GHz with 3.1 mW, and larger than 2 mW within the band between 219 and 227 GHz.

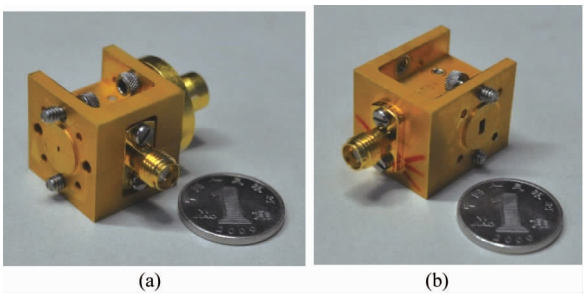

Fig. 3 (a) Tripler, (b) Mixer

图 3 (a) 三倍频器实物图, (b) 混频器实物图

The tripler is followed by a 440 GHz sub-harmonic mixer[18], as shown in Fig. 3(b). The key component in the mixer is an anti-parallel pair of Schottky diodes. The lengths of the diodes are 74 μm, and the cutoff frequency of the diodes is up to 8 000 GHz. The suspended microstrip matching circuit was constructed out of quartz, and the metal block was divided into two halves. The diode package and the matching circuit were integrated into the mixer. The measured results indicate that the mixer loss is below 17.0 dB in the band ranging from 433 to 451 GHz with a 3 dB bandwidth of 18 GHz.

The digital part is a high-speed digital correlator. The phase synchronization problem was solved with a cross synchronization scheme, based on a low cost FPGA controller. After digital quantization, a quadrature digital down converter was used before the complex correlation. The sampling rate of the correlator can be as high as 5 GHz, the effective number of the ADC is 6 bits[23], and the integration time is adjustable.

2.2 Point-source calibration

The proposed SMMW interferometric radiometer was demonstrated by a two-element interferometer. Therefore, the errors that originate in the receiver pairs can be regarded as simple modulations of the source images as long as the errors do not change during an imaging period, which can be guaranteed by this system. The most crucial errors arise from the bending and stretching of the flexible coaxial cables during the T-shaped scanning, as shown in Fig. 2. In order to reduce these errors, a point-source calibration method is presented in this paper.

The system repeats the same moving trajectory during every imaging period. The errors caused by the flexible coaxial cables can be described as a function of the coordinates in the spatial frequency domain. and indicate the magnitude and phase errors, respectively. Then Eq. 2 becomes,

$$V(u,v) = \iint_{\xi^2+\eta^2\leqslant 1} \frac{T(\xi,\eta) - T_r}{\sqrt{1-\xi^2-\eta^2}} F_{1,2*}(\xi,\eta)\tilde{r}_{1,2} \left(-\frac{u\xi - v\eta}{f_0}\right) e^{-j2\pi(u\xi - v\eta)} A(u,v)\varphi(u,v)\,d\xi d\eta \quad (3)$$

Considering a point-source target located at , we have:

$$V(u,v;\xi_0,\eta_0) = \iint_{\xi^2+\eta^2\leqslant 1} \frac{\delta(\xi-\xi_0,\eta-\eta_0)+T_p-T_r}{\sqrt{1-\xi^2-\eta^2}} F_{1,2}{}^*(\xi,\eta)$$
$$\tilde{r}_{1,2}\left(-\frac{u\xi+v\eta}{f_0}\right) e^{-j2\pi(u\xi+v\eta)} A(u,v)\varphi(u,v)\,d\xi d\eta \quad ,(4)$$

in which T_p is the background brightness of the point-source. A flat target response, $V(u,v;T_p-T'_r)$, can be obtained by turning off the point-source,

$$V(u,v;T_p-T'_r) = \iint_{\xi^2+\eta^2\leqslant 1} \frac{T_p-T_r}{\sqrt{1-\xi^2-\eta^2}} F_{1,2}{}^*(\xi,\eta)$$
$$\tilde{r}_{1,2}\left(-\frac{u\xi+v\eta}{f_0}\right) e^{-j2\pi(u\xi+v\eta)} A(u,v)\varphi(u,v)\,d\xi d\eta \quad , \quad (5)$$

in which T'_r is the instrument temperature during flat target imaging[24] that may vary from other imaging. The flat target response will be used as the flat target calibration for Eq. 4:

$$V'(u,v;\xi_0,\eta_0) = V(u,v;\xi_0,\eta_0) - \frac{T_r-T_p}{T'_r-T'_p} V(u,v;T_p-T')$$
$$= \iint_{\xi^2+\eta^2\leqslant 1} \frac{\delta(\xi-\xi_0,\eta-\eta_0)}{\sqrt{1-\xi^2-\eta^2}} \tilde{r}_{1,2}\left(-\frac{u\xi+v\eta}{f_0}\right)$$
$$F_{1,2}{}^*(\xi,\eta) e^{-j2\pi(u\xi+v\eta)} A(u,v)\varphi(u,v)\,d\xi d\eta \quad , \quad (6)$$

when $(\xi_0,\eta_0)\approx(0,0)$, $\sqrt{1-\xi^2-\eta^2}\approx 1$. The influence of the fringe washing function, $\tilde{r}_{1,2}$, can be neglected. The weighting effect of the antenna pattern becomes a constant that is approximately equal to one, which can also be ignored. Then Eq. 6 can be used as the point-source calibration for a common measurement, as described in Eq. 3, which leads to Eq. 7:

$$V'(u,v) = \frac{T(u,v)}{V'(u,v;\xi_0,\eta_0)} V$$
$$= \iint_{\xi^2+\eta^2\leqslant 1} \frac{T(\xi,\eta)-T_r}{\sqrt{1-\xi^2-\eta^2}} \tilde{r}_{1,2}\left(-\frac{u\xi+v\eta}{f_0}\right)$$
$$F_{1,2}{}^*(\xi,\eta) e^{-j2\pi[u(\xi+\xi_0)+v(\eta-\eta_0)]} d\xi d\eta \quad , \quad (7)$$

where the calibrated result $V'(u,v)$ can be regarded as a space shift of the raw $V(u,v)$.

Furthermore, the relationship between the flat target transformation and the point-source target transformation is notable. The Dirac delta function and the constant function are a Fourier transform pair in the theory of the Fourier transform. In this case, the visibility function of the flat target is approximately equal to the delta function, and the visibility function of the point-source target is similar to the constant function.

In practical applications, a flat target calibration is an additive operation that is intended to minimize the impact of antenna errors by minimizing $T(\xi,\eta)-T_r$, as described in Eq. 2, while a point-source calibration is a multiply operation used to eliminate multiplicative errors. These two calibrations do not interfere with each other; the flat target calibration assists the point-source calibration in eliminating the influence of the receiver noise temperature, as shown in Eq. 6.

Generally, a flat target calibration is effective for all synthetic aperture interferometric radiometers, and a point-source calibration is effective for a time-sharing system which has a scanning period. However, when point-source calibration is introduced into a complex system with a group of receivers, the inconsistency between the receivers should be considered, in Eqs. (6) and (7).

3 Experimental

3.1 Interferometric fringes experiment

When we fixed the interferometer and moved the point target, the interferometric fringes could be obtained as shown in Fig. 4(a). The phase of the interferometric fringes is shown in Fig. 4(b).

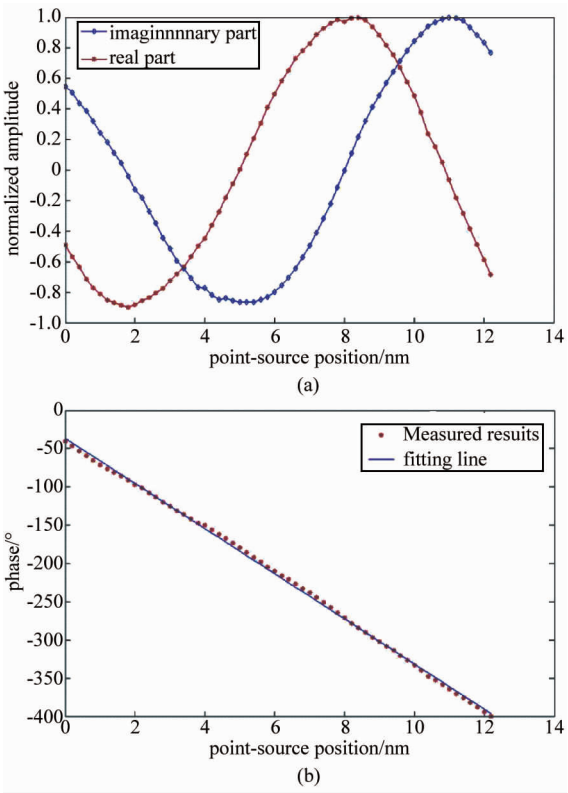

Fig. 4　(a) Interferometric fringes, (b) linear phase of the interferometric fringes

图 4　(a) 干涉条纹, (b) 干涉条纹的线性相位

During this experiment, the SMMW interferometer was operated at 440 GHz, the length of the baseline is 59.52 mm, and the distance between the interferometer and point-source is 1,100 mm. Using Eq. 1, the length of one interferometric fringe period was calculated to be 12.6 mm, while the measured value as shown in Fig. 4 is 12.4 mm. The linear correlation coefficient of the interferometric fringes is better than 0.999, and the corresponding linear phase error is less than 2°.

3.2 Point target imaging

When we fixed the point target and completed the spatial frequency domain sampling with the T-shape scanning, the point target image could be obtained with this SMMW interferometric radiometer.

During this experiment, the operated frequency is 440 GHz, and the longest baseline is 70λ in both direction ξ and η. The retrieved image without calibration is shown in Figs. 5(a) and (b), and the retrieved image with point-source calibration is shown in Figs. 5(c) and (d).

In terms of the theoretical analysis, the normalized synthetic aperture array factor function for an even sampling grid in the spatial frequency domain can be described as:

$$D(\xi,\eta) = \frac{\sin[(2N-1)\pi\Delta u\xi]}{(2N-1)\sin[\pi\Delta u\xi]} \cdot \frac{\sin(2M-1)\pi\Delta v\eta}{(2N-1)\sin[\pi\Delta u\xi]}, \quad (8)$$

in which Δu and Δv are the minimum antenna spacing normalized to the wave length in the directions of ξ and η, respectively. N and M are the number of antennas in the directions of ξ and η for no sparse array. The angle resolution can be defined as the 3 dB beam width of the synthetic aperture antenna pattern with reference to the real aperture system, derived from Eq. 8:

$$\theta_{HP\_\xi} \approx 1.207 \frac{1}{(2N-1)\Delta u}. \quad (9)$$

A similar result can be obtained in the direction of η.

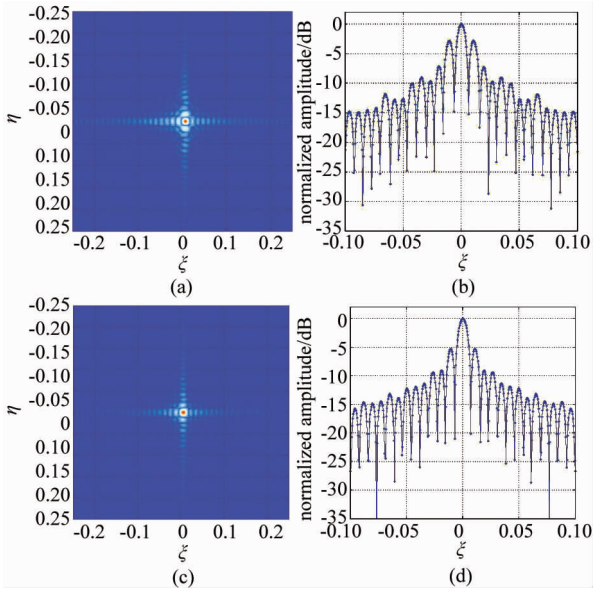

Fig. 5 Point target retrieved imaging (a) raw retrieved image, (b) cross-section of the raw retrieved image, (c) point-source calibrated image, and (d) cross-section of the calibrated image

图5 点源反演图 (a)原始数据反演图像,(b)原始反演图像的横剖图,(c)点源响应定标后数据的反演图像,(d)点源响应定标后反演图像的横剖图

A T-shape scanning array was used in this SMMW interferometric radiometer, and the equivalent antenna array corresponds to $N = M = 13$ and $\Delta u = \Delta v = 5$. By introducing these parameters into Eq. 8, we obtained a theoretical angle resolution of , and the ideal first sidelobe level approaches - 6.5 dB. The measured angle resolution is 0.565°, as shown in Fig. 5(c), which is in good agreement with the theoretical results. In the raw retrieved image, the first sidelobe level is - 2.8 dB, as shown in Fig. 5(a). After point-source calibration, the sidelobe level decreases to - 5.3 dB.

The experimental results show that point-source calibration plays a key role in reducing the first sidelobe, which is the reflection of the system errors in the synthetic aperture interferometric radiometer. Unfortunately, there is an obvious gap between the calibrated image and the theoretical image, which indicates the presence of significant errors in the point-source calibrated results. These errors will be addressed in future work.

4 Conclusion

An SMMW interferometric radiometer has been setup using a two-element interferometer at 440 GHz. A point-source calibration method has been proposed to improve its performance. The experimental results of interferometric fringes and point target images have been presented. The linear phase error of the interference fringes is less than 2°, while the angular resolution of the retrieved point target image is around 0.565°. The performance of the experimental system is in good agreement with theoretical calculations.

The technical feasibility of SMMW synthetic aperture imaging has been verified by this interferometer. In future works, the calibration method should be improved in order to reduce the remaining system errors. The design of a modified SMMW interferometric radiometer is currently in progress.

References

[1] Maestrini A, Ward J S, Gill J J, *et al*. A 540-640-GHz High-efficiency Four-anode frequency tripler[J]. *IEEE Transactions on Microwave Theory and Techniques*, 2005, **53**,(9): 2835 - 2843.

[2] Leong K, Mei X B, Yoshida W, *et al*. Progress in InP HEMT submillimeter wave circuits and packaging[C]. In IEEE Compound Semiconductor Integrated Circuit Symposium, New Orleans, LA, 2015, pp. 1 - 4.

[3] ZHANG Yue-Dong, JIANG Yue-Song, HE Yun-Tao, *et al*. Passive millimeter-wave imaging using photonic processing technology[J]. *J. Infrared Millim. Waves*(张跃东,江月松,何云涛,等. 基于光子学处理技术的被动毫米波成像,**红外与毫米波学报**),2011, **30**(6): 551 - 555.

[4] Luukanen A, Kiuru T, Leivo M M, *et al*. Passive three-colour submillimetre-wave video camera[J]. *Proc. of SPIE*, 2015, **8715**:87150F.

[5] Irimajiri Y, Manabe T, Ochiai S, *et al*. BSMILES—A balloon-borne superconducting submillimeter-wave limb-emission sounder for stratospheric measurements[J]. *IEEE Geoscience and Remote Sensing Letters*, 2006, **3**(1):

[6] Pickett H M, Poynter R L, Cohen E A. Submillimeter, millimeter, and microwave spectral line catalog[J]. *J. Quant. Spectrosc. Radiat. Transf.*, 1998, **60**(5):883 - 890.

[7] Waters J W, Froidevaux L, Harwood R S. The earth observing system microwave limb sounder (EOS MLS) on the aura satellite[J]. *IEEE Trans. Geosci. Remote Sens.*, 2006, **44**(5):1075 - 1092.

[8] Kikuchi K, Nishibori T, Ochiai S. Overview and early results of the superconducting submillimeter-wave limb-emission sounder (SMILES)[J]. *J. Geophys. Res.*, 2010,**115**(D23):D23306 - 1 - D23306 - 12.

[9] Liu H, Wu J, Zhang S W. Conceptual design and breadboarding activities of geostationary interferometric microwave sounder (GIMS)[J]. In Proc. IGARSS, Cape Town, South Africa, 2009, pp. 1039 - 1042.

[10] Zhang C, Liu H, Wu J, *et al*. Imaging analysis and first results of the geostationary interferometric microwave sounder demonstrator[J]. *IEEE Trans. Geosci. Remote Sens.*, 2015, **53**(1):207 - 218.

[11] Read W G, Shippony Z, Schwartz M J, *et al*. The clear-sky unpolarized forward model for the EOS aura microwave limb sounder (MLS)[J]. *IEEE Trans. Geosci. Remote Sens.*, 2006, **44**(5): 1367 - 1379.

[12] Rodriguez-Morales F, Yngvesson K S, Gerecht E. A terahertz focal

plane array using HEB superconducting mixers and MMIC IF amplifiers [J]. *IEEE Microw. Compon. Lett.*, 2005, **15**(4): 199 - 201.

[13] Ruf C S, Swift C T, Tanner A B, *et al*. Interferometric synthetic aperture microwave radiometry for the remote sensing of the Earth [J]. *IEEE Trans. Geosci. Remote Sens.*, 1998, **26**(5): 597 - 611.

[14] Brown M A, Torres F, Corbella I, *et al*. SMOS calibration [J]. *IEEE Trans. Geosci. Remote Sens.*, 2008, **46**(3): 646 - 658.

[15] Corbella I, Torres F, Camps A, *et al*. MIRAS end-to-end calibration: Application to SMOS L1 Processor [J]. *IEEE Trans. Geosci. Remote Sens.*, 2005, **43**(5): 1126 - 1134.

[16] Tanner A B, Wilson W J, Lambrigsten B H. Initial results of the geostationary synthetic thinned array radiometer (GeoSTAR) demonstrator instrument [J]. *IEEE Trans. Geosci. Remote Sens.*, 2007, **45**(7): 1947 - 1957.

[17] MENG Jing, ZHANG De-Hai, JIANG Chang-Hong, *et al*. Research on the practical design method of 225 GHz tripler [J]. *J. Infrared Millim. Waves* (孟进, 张德海, 蒋长宏, 等. 225 GHz 三倍频器实用设计方法, **红外与毫米波学报**), 2015, **34**(2): 190 - 195.

[18] ZHAO Xin, JIANG Chang-Hong, Zhang De-Hai, *et al*. Design of the 450 GHz sub-harmonic mixer based on Schottky diode [J]. *J. Infrared Millim. Waves* (赵鑫, 蒋长宏, 张德海, 等. 基于肖特基二极管的450GHz 二次谐波混频器, **红外与毫米波学报**), 2015, **34**(3): 301 - 306.

[19] Corbella I, Duffo N, Vall-llossera M. The visibility function in interferometric aperture synthesis radiometry [J]. *IEEE Trans. Geosci. Remote Sens.*, 2004, **42**(8): 1677 - 1682.

[20] Butora R, Neira M M, Luis A, *et al*. Fringe-washing function calibration in aperture synthesis microwave radiometry [J]. *Radio Science*, 2003, **38**(2): 15 - 1.

[21] Camps A, Bara J, Corbella I, *et al*. The processing of hexagonally sampled signals with standard rectangular techniques: Application to 2-D large aperture synthesis interferometric radiometers [J]. *IEEE Trans. Geosci. Remote Sens.*, 1997, **35**(1): 183 - 190.

[22] Zhang C, Wu J, Sun W Y. Applications of pseudo-polar FFT in synthetic aperture radiometer imaging [J]. *PIERS Online*, 2007, **3**(1).

[23] WU Qiong-Zhi, CAI Chun-Xia, DING Yi-Chen, *et al*. Design and implementation of 5Gsps high-speed data acquisition system [J]. *Electronic Design Engineering* (吴琼之, 蔡春霞, 丁一辰, 等. 5Gsps 高速数据采集系统的设计与实现, **电子设计工程**), 2012, **20**(1): 154 - 157.

[24] Neira M M, Suess M, Kainulainen J. The flat target transformation [J]. *IEEE Trans. Geosci. Remote Sens.*, 2008, **46**(3): 613 - 620.